



Multiscale modeling of fiber recruitment and damage with a discrete fiber dispersion method

Kewei Li^a, Gerhard A. Holzapfel^{a,b,*}

^a Institute of Biomechanics, Graz University of Technology Stremayrgasse 16-II, Graz 8010, Austria

^b Department of Structural Engineering, Norwegian University of Science and Technology, Trondheim 7491, Norway

ARTICLE INFO

Article history:

Received 31 October 2018

Revised 25 January 2019

Accepted 31 January 2019

Available online 5 February 2019

Keywords:

Fiber recruitment and damage

Discrete fiber dispersion model

Exclusion of compressed fibers

Constitutive modeling

Finite element analysis

ABSTRACT

Recently, we introduced a discrete fiber dispersion model based on triangular discretization of a unit sphere with a finite number of elementary areas. Over each elementary area, we define a representative fiber direction and an elementary fiber density based on the fiber dispersion. The strain energy of fibers distributed in each elementary area is then approximated by the deformation of the representative fiber direction weighted by the corresponding elementary fiber density. A summation of fiber contributions of all elementary areas yields the resultant fiber strain energy. However, in that study we did not consider fiber recruitment, softening and damage. The goal of this study is to incorporate these important properties of collagen fibers into the constitutive model. We first define a fiber recruitment stretch at which the fiber becomes straightened. Then, we adopt the continuum damage mechanics method for modeling fiber softening and damage. We implemented the proposed model in a finite element program and verified it with three representative examples including a uniaxial extension test of a dog-bone shaped specimen up to failure. The computational solution agrees well with the experimental result. In conclusion, the proposed model is able to capture fiber recruitment, softening, and damage. Future studies with more complex boundary conditions are necessary to verify this approach.

© 2019 Elsevier Ltd. All rights reserved.

1. Introduction

Since the microstructurally-motivated constitutive modeling was introduced to the soft tissue mechanics field in 1970s, there have been tremendous interest and development in this area (Lanir, 2018). Especially with the advance of imaging techniques such as second-harmonic generation (SHG), which has enabled detailed visualization of the underlying microscopic constituents such as collagen fibers of arterial tissues (Niestrawska et al., 2016; Schriefel et al., 2013; 2012), continuum mechanics-based multiscale constitutive models have also been evolving in the last few decades so that more and more details of the underlying tissue microstructure can be accounted for (Gasser et al., 2006; Holzapfel et al., 2000, 2015; Holzapfel and Ogden, 2010; Lanir, 1983; Li et al., 2016, 2018a, 2018c). In particular, multiscale constitutive models that incorporate the three-dimensional (3D) fiber dispersion in fibrous tissues have gained a lot of momentum in the last decade and have been employed extensively to model the mechanical response of these tissues (Gasser et al., 2006). However, most of those multiscale constitutive models were proposed for the elastic tissue behavior under physiological loading condition.

* Corresponding author at: Institute of Biomechanics, Graz University of Technology Stremayrgasse 16-II, Graz 8010, Austria.
E-mail address: holzapfel@tugraz.at (G.A. Holzapfel).

In some surgical procedures such as balloon angioplasty or arterial clamping, patients also experience supra-physiological loading conditions which may cause tissue damage or tear (Fereidoonzhad et al., 2016). In addition, aortic dissection or rupture may lead to a high risk of mortality among patients with ascending thoracic aortic aneurysms. Thus, both tissue damage and rupture occur in patients. But microstructurally-motivated constitutive models that account for such complex inelastic tissue softening, damage and rupture are rare.

Because collagen fibers in fibrous tissues govern the mechanical behavior of the tissues once “activated”, modeling the tissue softening and damage requires a deep understanding of the fiber properties and how fibers affect the tissue behavior. Due to their waviness and slenderness, collagen fibers bear non-zero stress only when straightened, thus, there is no fiber contribution to the tissue deformation in the low strain range. Gradual uncrimping and recruitment of dispersed and wavy fibers also induce the nonlinear and anisotropic behavior of soft fibrous tissue. In the high strain range fiber softening, for example, due to sliding of collagen fibrils or damage of interfibrillar proteoglycan bridges (Gasser, 2011; Schmidt et al., 2014), and fiber rupture also cause tissue softening and failure. The viscoelastic behavior of fibrous tissue is also attributed to the properties of collagen fibers (Lanir, 2018) but is not considered in this study.

Continuum constitutive models that consider such complex and inelastic fiber properties have been proposed for either fiber recruitment or fiber damage. But they are often rather limited in some aspects when incorporating the microscale fiber recruitment, softening, and damage process into the macroscale tissue behavior. At the microscopic scale, collagen fibers are often crimped in the stress-free configuration. Thus, they do not bear stress under compression or before being uncrimped. The fiber recruitment stretch is defined as a critical stretch value at which a fiber becomes uncrimped (straightened) and starts to bear stress. Currently, there are a number of constitutive laws proposed specifically for modeling fiber uncrimping and recruitment. For example, our group has previously proposed a constitutive law for modeling the recruitment of dispersed fibers (Weisbecker et al., 2015). The authors assumed there are a number of fibers with varying waviness in each orientation over the unit sphere. The recruitment stretches of those fibers distributed in the same orientation were described by the beta distribution function. Then, the strain energy of all the fibers distributed in the same direction was determined by an integration of the single fiber strain-energy function over all the fibers weighted by the recruitment distribution function. With that, the strain-energy function of all the fibers over the unit sphere can be calculated by an integration of the fiber strain energy over all the orientations weighted by a fiber probability density function (PDF). Similarly, motivated by the pioneering work of Lanir (1983), another study examined the influence of different distribution functions of fiber recruitment stretch on the tissue response (Hill et al., 2012). The authors compared the gamma distribution function and the step function for fiber recruitment. Through extensive examination of multi-photon microscopic images of the fiber recruitment and stretching under different deformation states, the authors were able to identify the fiber recruitment and eventually fit the experimental data with the proposed model by using both methods (gamma distribution function and neo-Hookean model or step function and exponential model). Both studies considered that the recruitment function, either a distribution function or a step function, is the same for all the fiber orientations over the distributed domain or plane, although theoretically it is possible to define different recruitment functions for different fiber orientations.

Besides, there are several studies that focus on tissue damage due to microscale fiber softening and damage. In general, the modeling of damage in soft fibrous tissues can be accomplished by using three methods (Holzapfel and Fereidoonzhad, 2017), the continuum damage mechanics (CDM) approach (Holzapfel, 2000; Simo, 1987), the theory of pseudo-elasticity (Dorfmann and Ogden, 2004; Fung et al., 1979; Ogden and Roxburgh, 1999), and the softening hyperelasticity approach (Volokh, 2007; 2008; 2011). Following the suggestions in Holzapfel and Fereidoonzhad (2017), we focus on the CDM method in this study because it can capture the failure region of stress versus stretch curve as a result of bond rupture or complete tissue damage as well as the Mullins effect and the hysteresis behavior of tissues. Thus, it has been extensively applied for modeling of tissue damage (Calvo et al., 2007; Holzapfel and Fereidoonzhad, 2017), and recently in the framework of microsphere-based method for modeling fiber damage (Sáez et al., 2012). In that study, the CDM approach was applied on each of the integration directions over the sphere. The computational homogenization of the matrix and fiber responses was achieved by using a numerical integration scheme. Overall, the method is capable of fitting the uniaxial extension test data by using one element and simulating the vessel inflation with a simplified model up to failure. A more recent study (Schmidt and Balzani, 2016) has extended this method to model the atherosclerotic artery with a more realistic geometry under inflation test.

Other than the microsphere-based approach, a similar method was also proposed for modeling irreversible fiber damage in abdominal aortic aneurysms by using spherical t -designs (Gasser, 2011). A spherical t -design is a type of numerical method used to approximate the integration of polynomial functions over the unit sphere. With a finite number of evenly distributed points over the unit sphere, the method aims to integrate polynomial functions up to degree t exactly. Since the existing numerical integration methods, either in the microsphere-based approach or the spherical t -design, were specifically proposed for polynomial functions over the entire unit sphere (Ehret et al., 2010), for the actual fiber distribution measured from the imaging analysis of aortic tissues (Niestrawska et al., 2016), the integrand may be much more complex. Furthermore, if the exclusion of fibers under compression is considered, then the numerical integration should be performed over a subdomain of the unit sphere (Li et al., 2016), resulting that only part of the integration points are used in the numerical integration for computation of stress and elasticity tensors. The accuracy of the numerical integration over a subdomain of sphere by using part of the integration points is questionable because the existing numerical integration schemes over the unit sphere were only developed for the entire sphere. Thus, as pointed out by Lanir in a recent review (Lanir, 2018), it is still questionable whether those methods are accurate enough to approximate the integration of an actual fiber dispersion

and complex strain-energy functions within a subdomain of the unit sphere appearing in the constitutive models of fibrous tissues.

In addition, a macroscale volume-averaged stress balance method was also proposed for computational homogenization of the matrix and fiber stresses in the failure modeling of ascending thoracic aorta (Shah et al., 2014). Although the experimental and computationally predicted first Piola–Kirchhoff stress versus stretch curves are similar in both uniaxial and biaxial tests, fiber softening was not considered in the constitutive model, and fiber damage was only accounted for in the constitutive model by reducing the fiber Young's modulus to a number close to zero once its stretch reaches a critical value. This critical fiber stretch was a fitting material parameter and was not based on any experimental tests. The in-plane fiber rotation in the uniaxial test simulation of the axial specimen seems to be unrealistically large, because if fibers are aligned in the circumferential direction, they should be under compression when the specimen is loaded in the axial direction. They should not rotate and engage in tension. As the authors pointed out, the free rotation of fibers overestimated the fiber's capacity to rotate.

Thus, a constitutive model that incorporates the fiber recruitment, softening and damage and can efficiently exclude compressed fibers from a dispersion without dependence on specific numerical integration schemes is lacking. In this study, we extend our recently proposed discrete fiber dispersion (DFD) model (Li et al., 2018a) to consider the microscale fiber recruitment, softening, and damage process so that the tissue softening and damage can also be captured. Briefly, in the DFD model (Li et al., 2018a) we first convert the continuous fiber PDF over the unit sphere into a finite number of elementary fiber densities through triangular discretization of a unit sphere into a finite number of elementary areas. For each elementary area, we also define a representative fiber direction at the centroid of that area. Then, the strain energy of all the fibers within an elementary area is calculated by using the deformation in the representative fiber direction weighted by the corresponding elementary fiber density. A summation of fiber contributions of all elementary areas yields the resultant fiber strain energy. This treatment allows us to exclude fibers under compression directly (Li et al., 2018a). However, in that study, the fiber uncrimping, recruitment, softening and damage were not considered. Therefore, the goal of the current study is to incorporate those inelastic fiber properties into the DFD model. To accomplish that, we first define a fiber recruitment stretch at which fibers start to bear load. We then adopt the CDM approach (Holzapfel, 2000; Holzapfel and Fereidoonzhad, 2017) for modeling of damage in the fiber and matrix material. Thus, a damage variable is introduced for each representative fiber direction and the matrix material. We implemented the proposed constitutive model in a finite element program, and through three representative examples we demonstrate the effects of fiber recruitment and damage on the overall tissue behavior.

The present paper is structured as follows. In Section 2 we present a brief review of the DFD model and then the continuum mechanical framework of the proposed damage model based on the DFD model including the incorporation of fiber recruitment, modeling of fiber and matrix damage, the final form of strain-energy function, and the Cauchy stress and elasticity tensors in a decoupled form. In Section 3 we specialize the fiber distribution to a rotationally symmetric dispersion by using the von Mises distribution for illustration of the method. Besides, a specific form of the single fiber strain-energy function is also introduced. The theory introduced in Section 2 and details of the model provided in Section 3 are then applied to several representative examples in Section 4 with the aim of demonstrating the efficacy and efficiency of the proposed model. Finally, Section 5 summarizes the proposed constitutive modeling approach and suggests some future research areas.

2. Continuum mechanical framework

In this section, we present the continuum mechanical framework of the proposed constitutive model considering fiber recruitment, softening and damage. The strain-energy function, the corresponding Cauchy stress and elasticity tensors are given in a decoupled form for efficient finite element implementation.

2.1. Kinematics

We first introduce a deformation map $\mathbf{x} = \chi(\mathbf{X})$ which transforms a material point \mathbf{X} in the stress-free, reference configuration into a spatial point \mathbf{x} in the deformed configuration. The deformation gradient is then defined as $\mathbf{F}(\mathbf{X}) = \partial \chi(\mathbf{X}) / \partial \mathbf{X}$, and its determinant $J = \det \mathbf{F}(\mathbf{X}) > 0$ represents the local volume ratio at point \mathbf{X} , with $J \equiv 1$ representing a strictly incompressible material. Following the multiplicative decomposition of the deformation gradient (Flory, 1961; Ogden, 1978), we decouple \mathbf{F} into a volumetric (dilatational) part $J^{1/3} \mathbf{I}$ and an isochoric (distortional) part $\bar{\mathbf{F}} = J^{-1/3} \mathbf{F}$, with $\det \bar{\mathbf{F}} \equiv 1$. Based on \mathbf{F} we define the right Cauchy–Green tensor as $\mathbf{C} = \mathbf{F}^T \mathbf{F}$ and its isochoric counterpart as $\bar{\mathbf{C}} = \bar{\mathbf{F}}^T \bar{\mathbf{F}}$, with the corresponding first invariants defined by

$$I_1 = \text{tr} \mathbf{C}, \quad \bar{I}_1 = \text{tr} \bar{\mathbf{C}}, \quad (1)$$

respectively. If \mathbf{N} is a given constant vector in the reference configuration, then $\mathbf{C} : \mathbf{N} \otimes \mathbf{N}$, denoted I_4 , represents the square of the material stretch in the direction \mathbf{N} . Its isochoric counterpart is denoted \bar{I}_4 . Hence,

$$I_4 = \mathbf{C} : \mathbf{N} \otimes \mathbf{N}, \quad \bar{I}_4 = \bar{\mathbf{C}} : \mathbf{N} \otimes \mathbf{N}. \quad (2)$$

Let us now introduce unit Cartesian basis vectors $\mathbf{E}_1, \mathbf{E}_2, \mathbf{E}_3$ and then express \mathbf{N} in terms of spherical polar angles Θ and Φ relative to $\mathbf{E}_1, \mathbf{E}_2, \mathbf{E}_3$ such that

$$\mathbf{N} = \sin \Theta \cos \Phi \mathbf{E}_1 + \sin \Theta \sin \Phi \mathbf{E}_2 + \cos \Theta \mathbf{E}_3. \quad (3)$$

2.2. Discrete modeling of fiber dispersion

The discrete treatment of fiber dispersion has been previously established (Li et al., 2018a). Briefly, we begin with the strain-energy function Ψ_f of fibers per unit volume in the reference configuration, defined in the continuous fiber dispersion (cFD) model (Li et al., 2016), i.e.

$$\Psi_f = \frac{1}{2\pi} \int_{\mathbb{S}} \rho(\Theta, \Phi) \Psi_n(I_4) \sin \Theta d\Theta d\Phi, \quad (4)$$

where we assume that the 3D fiber dispersion inside the matrix material can be described by an integrable function $\rho(\Theta, \Phi)$ defined over the unit hemisphere $\mathbb{S} = \{(\Theta, \Phi) \mid \Theta \in [0, \pi], \Phi \in [0, \pi]\}$, $\Psi_n(I_4)$ represents the single fiber strain energy in the direction of $\mathbf{N}(\Theta, \Phi)$. We require

$$\Psi_n(1) = 0, \quad \Psi'_n(1) = 0. \quad (5)$$

Note that it is only necessary to integrate over the unit hemisphere because the directions \mathbf{N} and $-\mathbf{N}$ represent the same fiber within a dispersion.

Then, we discretize the unit hemisphere \mathbb{S} into a finite number of elementary areas $\Delta\mathbb{S}_n, n = 1, \dots, m$, where m denotes the number of elementary areas over the hemisphere. An example of such a discretization with spherical triangles is shown in Fig. 1 of Li et al. (2018a). Over each elementary area, we define a representative fiber direction (Θ_n, Φ_n) at the centroid of the elementary area and an elementary fiber density. The physical meaning of the elementary fiber density is the normalized number of fibers within each elementary area, which can be determined by

$$\rho_n = \frac{1}{2\pi} \int_{\Delta\mathbb{S}_n} \rho(\Theta, \Phi) \sin \Theta d\Theta d\Phi, \quad n = 1, \dots, m. \quad (6)$$

We only require $\rho(\Theta, \Phi)$ to be an integrable function over $\Delta\mathbb{S}_n$. If it is a discontinuous function over the hemisphere, then a special discretization scheme could be readily employed such that $\rho(\Theta, \Phi)$ is integrable locally over each $\Delta\mathbb{S}_n$. The elementary fiber density ρ_n must satisfy the normalization condition, i.e.

$$\sum_{n=1}^m \rho_n = 1. \quad (7)$$

We assume one family of fibers embedded in the matrix material in (4). If additional fiber families are present in the tissue, they can be included additively in a straightforward way, with different structural and material parameters, in general, see the third example in Li et al. (2018b). If the fibers in the additional family have the same property as those in the first one, then it can also be added to (6) directly as

$$\rho_n = \frac{1}{2\pi} \int_{\Delta\mathbb{S}_n} (\rho(\Theta, \Phi) + \varrho(\Theta, \Phi)) \sin \Theta d\Theta d\Phi, \quad n = 1, \dots, m, \quad (8)$$

where $\varrho(\Theta, \Phi)$ denotes the fiber PDF of the second fiber family. As defined in (6), the value of ρ_n depends on the area of integration domain $\Delta\mathbb{S}_n$ and the fiber density over that area. Depending on the actual fiber distribution, the areas of the $\Delta\mathbb{S}_n, n = 1, \dots, m$, could be defined such that an optimal integration result is achieved. For example, regions with higher fiber density could be discretized with smaller $\Delta\mathbb{S}_n$. However, in this study, for the purpose of demonstration, we choose the triangular type of discretization shown in Fig. 1 of Li et al. (2018a) which yields nearly constant elementary areas.

2.3. Modeling fiber recruitment

The arrangement and morphology of collagen fibers inside the ground substance vary significantly from tissue to tissue (Niestrawska et al., 2016; Schriefel et al., 2013; 2012; Zuo et al., 2016). But it is often observed that fibers exhibit a certain degree of waviness. Frequently, we assume that the straightening of fibers from a wavy (crimped) state to a straightened state involves no stress accumulation in the fiber, see Fig. 1(a),(b). Beyond that, fibers start to contribute to the strain-energy function of the tissue. In the framework of the discrete treatment, we can model this behavior by defining a true fiber stretch λ_n in any representative fiber direction \mathbf{N}_n as

$$\lambda_n = \lambda_f / \lambda_r, \quad (9)$$

where λ_f denotes the current fiber stretch, and λ_r defines the critical fiber recruitment stretch at which the fiber becomes straightened but does not bear any stress (Hill et al., 2012). A further stretch of the fiber ($\lambda_n > 1$) induces stress. Note that the fiber recruitment stretch λ_r is a material property and can be measured by imaging analysis.

In the current discrete treatment, λ_r can be interpreted as an average fiber recruitment stretch defined in the representative fiber direction. Because within each elementary area the fiber waviness may vary, the average fiber recruitment

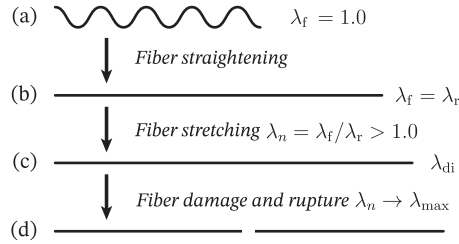


Fig. 1. Deformation of a single collagen fiber from the initially crimped state to an intermediate stress-free state and to the final ruptured state. The current fiber stretch λ_f is determined by using I_4 defined in (2). (a) In the reference configuration, the current fiber stretch λ_f is 1.0, (b) after straightened but still stress free, the current fiber stretch is defined as the critical fiber stretch, also the true fiber stretch $\lambda_n = 1$ at this stage, (c) an intermediate stressed state with a stretch of λ_{di} representing the damage initiation in the fiber; prior to that, the fiber deformation is purely elastic, and (d) the final ruptured state λ_{max} . Note that the damage initiation stretch λ_{di} and the maximum fiber stretch λ_{max} are defined with respect to the true fiber stretch λ_n .

stretch accounts for such variation so that the strain energy induced in all the fibers within an elementary area at each deformation state is equivalent to the strain energy of the representative fiber direction defined in this model. Thus, it is not necessary to multiply a distribution function of fiber recruitment stretch by the strain-energy function of the representative fiber direction in this model. Mathematically, it can be considered that the strain energy Ψ_n of the representative fiber direction in the current study is equivalent to the integration of the single fiber strain energy over all the fiber directions within the elementary area weighted by a distribution function of the fiber recruitment stretch, see Section 2.2.2 of Weisbecker et al. (2015) and Hill et al. (2012). Certainly, if the waviness of the fibers distributed in each elementary area is known (Roy et al., 2010), a distribution function of the fiber recruitment stretch could be determined and incorporated in the DFD model, as was described in our previous study (Weisbecker et al., 2015). It could also be approximated as an average value of several fiber orientations measured over each elementary area. The distribution of fiber recruitment stretch over the unit hemisphere can be anisotropic or isotropic. But, without loss of generality, we assume it is isotropic in the first two examples for illustration purposes. In the last example, we then use a variable fiber recruitment stretch.

With the discrete treatment of fiber dispersion over the unit hemisphere, we then re-define the strain-energy function (4) for all the fibers per unit volume in the reference configuration as

$$\Psi_f = \sum_{n=1}^m \rho_n \Psi_n(\lambda_n^2), \quad (10)$$

where $\lambda_n^2 = \lambda_f^2 / \lambda_r^2$ and $\lambda_f^2 = I_{4n} = \mathbf{C} : \mathbf{N}_n \otimes \mathbf{N}_n$ is defined for the representative fiber direction \mathbf{N}_n of each elementary area via (3) with $\Theta = \Theta_n$ and $\Phi = \Phi_n$. Now, in order to exclude all the fibers under compression and crimped fibers within a dispersion, we define Ψ_n as

$$\Psi_n(\lambda_n^2) = \begin{cases} f(\lambda_n^2) & \text{if } \lambda_n^2 \geq 1, \\ 0 & \text{if } \lambda_n^2 < 1, \end{cases} \quad (11)$$

where $f(\lambda_n^2)$ represents the strain-energy function of a single fiber under tension and satisfies $f(1) = f'(1) = 0$, $f(\lambda_n^2) > 0$ and $f'(\lambda_n^2) > 0$ for $\lambda_n^2 > 1$. Those requirements ensure a smooth transition of the fiber stress versus stretch curve from the crimped state to the stressed state.

Following the decomposed form of the deformation gradient, we can also write the strain-energy function in a decoupled form, namely

$$\Psi = \Psi_{vol} + \Psi_{iso}, \quad (12)$$

where Ψ_{vol} describes the volumetric deformation and Ψ_{iso} the isochoric deformation. We further decompose the isochoric contribution into two parts,

$$\Psi_{iso} = \Psi_g + \Psi_f, \quad (13)$$

where Ψ_g denotes the isochoric strain energy of the ground substance, which is assumed to be isotropic and to depend only on \bar{I}_1 . Then, from (10) and (13) we have

$$\Psi_{iso} = \Psi_g(\bar{I}_1) + \sum_{n=1}^m \rho_n \Psi_n(\bar{\lambda}_n^2), \quad \Psi_n(\bar{\lambda}_n^2) = \begin{cases} f(\bar{\lambda}_n^2) & \text{if } \bar{\lambda}_n^2 \geq 1, \\ 0 & \text{if } \bar{\lambda}_n^2 < 1, \end{cases} \quad (14)$$

where $\bar{\lambda}_n^2 = \bar{\lambda}_f^2 / \lambda_r^2$ and $\bar{\lambda}_f^2 = \bar{I}_{4n} = \bar{\mathbf{C}} : \mathbf{N}_n \otimes \mathbf{N}_n$. For strictly incompressible materials we have $\lim_{j \rightarrow 1} \bar{I}_{4n} = I_{4n}$.

In our previous experimental study (Weisbecker et al., 2013), it has been shown that it is sufficient to use a neo-Hookean model for the non-collagenous matrix material. Thus,

$$\Psi_g(\bar{I}_1) = \frac{\mu}{2} (\bar{I}_1 - 3), \quad (15)$$

where the constant $\mu (> 0)$ is the shear modulus and \bar{I}_1 is given in (1)₂.

Since our primary focus is on the constitutive modeling of incompressible materials, the volumetric strain-energy function is used as a penalty function, and it is convenient to adopt a form for Ψ_{vol} given in the FEAP manual (Taylor, 2013), i.e.

$$\Psi_{\text{vol}} = \frac{K}{4}(J^2 - 1 - 2\ln J), \quad (16)$$

where K is a penalty parameter. The derivations of the volumetric parts of the stress and elasticity tensors are straightforward and have been well documented (Gasser et al., 2006; Holzapfel, 2000). Hence, in the following we only derive the isochoric parts of the stress and elasticity tensors.

2.4. Modeling fiber and matrix damage

If fibers are continuously loaded after they are “straightened”, micro-cracks may initiate inside the fiber, or breakage of interfibrillar proteoglycan bridges (Schmidt et al., 2014) may occur. Thus, they eventually rupture at some point. Since the damage/rupture is irreversible, the damaged/ruptured fiber loses its load-bearing capability permanently, see Fig. 1. As discussed in Section 1, in this study we adopt the cDM method for modeling fiber and matrix damage. Following the cDM method, we introduce the damage variables d_g and d_n for the ground substance and each representative fiber direction, respectively, in (14)₁, i.e.,

$$\Psi_{\text{iso}} = (1 - d_g)\Psi_g + \sum_{n=1}^m \rho_n(1 - d_n)\Psi_n, \quad (17)$$

where $(1 - d_g)$ and $(1 - d_n)$, $n = 1, \dots, m$, are so-called reduction factors (Simo, 1987) for the ground substance and the fibers, respectively, Ψ_g and Ψ_n now denote the effective strain-energy functions of the hypothetically undamaged matrix material and fibers, respectively. Note that we assume that damage initiation and evolution only occur due to the isochoric deformation of the material, because the volumetric part vanishes as $J \rightarrow 1$ for incompressible material. The inelastic degradation phenomena of the ground substance and fibers introduced by the reduction factors $(1 - d_g)$ and $(1 - d_n)$ satisfy $0 \leq d_g \leq 1$ and $0 \leq d_n \leq 1$, $n = 1, \dots, m$, respectively. The condition $d_g = 0$ or $d_n = 0$ represents undamaged (elastic) state of the material, while $d_g = 1$ or $d_n = 1$ represents complete material damage due to bound rupture or breakage of proteoglycan bridges.

In order to determine the stress relation and internal energy dissipation we apply the standard Coleman–Noll procedure (Holzapfel, 2000; Simo, 1987). At first, we differentiate the strain-energy function (12) with respect to time by using the chain rule

$$\dot{\Psi} = \left[\frac{\partial \Psi_{\text{vol}}}{\partial \mathbf{C}} + (1 - d_g) \frac{\partial \Psi_g}{\partial \mathbf{C}} + \sum_{n=1}^m \rho_n(1 - d_n) \frac{\partial \Psi_n}{\partial \mathbf{C}} \right] : \dot{\mathbf{C}} - \Psi_g \dot{d}_g - \sum_{n=1}^m \rho_n \Psi_n \dot{d}_n. \quad (18)$$

Then, we particularize the second law of thermodynamics through the Clausius–Plank inequality (Holzapfel, 2000) for an isothermal process, i.e.

$$\mathcal{D}_{\text{int}} = \mathbf{S} : \frac{\dot{\mathbf{C}}}{2} - \dot{\Psi} = \left[\mathbf{S} - 2 \frac{\partial \Psi_{\text{vol}}}{\partial \mathbf{C}} - 2(1 - d_g) \frac{\partial \Psi_g}{\partial \mathbf{C}} - 2 \sum_{n=1}^m \rho_n(1 - d_n) \frac{\partial \Psi_n}{\partial \mathbf{C}} \right] : \frac{\dot{\mathbf{C}}}{2} + \Psi_g \dot{d}_g + \sum_{n=1}^m \rho_n \Psi_n \dot{d}_n \geq 0, \quad (19)$$

where \mathcal{D}_{int} describes the internal dissipation which is required to be non-negative at any point inside the material for all the time. From that, we can deduce the second Piola–Kirchhoff stress tensor \mathbf{S} and a simplified expression for \mathcal{D}_{int} as

$$\mathbf{S} = \mathbf{S}_{\text{vol}} + \mathbf{S}_{\text{iso}}, \quad \mathbf{S}_{\text{vol}} = 2 \frac{\partial \Psi_{\text{vol}}}{\partial \mathbf{C}}, \quad \mathbf{S}_{\text{iso}} = 2(1 - d_g) \frac{\partial \Psi_g}{\partial \mathbf{C}} + 2 \sum_{n=1}^m \rho_n(1 - d_n) \frac{\partial \Psi_n}{\partial \mathbf{C}}, \quad (20)$$

$$\mathcal{D}_{\text{int}} = \Psi_g \dot{d}_g + \sum_{n=1}^m \rho_n \Psi_n \dot{d}_n \geq 0.$$

Clearly, the internal dissipation inequality (20)₄ shows that damage evolution is a dissipative process. In cDM, the quantities Ψ_g and $\rho_n \Psi_n$, $n = 1, \dots, m$, are thermodynamic forces conjugate to their corresponding damage variables. Those thermodynamic forces are non-negative functions and govern the damage evolution processes of the matrix material and fibers. This implies that the damage variables d_g and d_n , $n = 1, \dots, m$, must be monotonically increasing functions in order to fulfill the Clausius–Plank inequality (20)₄.

Following the damage model proposed in Simo (1987), we define the damage variables as functions of equivalent strains Ξ_g and Ξ_n ,

$$\Xi_g = \sqrt{2\Psi_g}, \quad \Xi_n = \sqrt{2\Psi_n}, \quad n = 1, \dots, m. \quad (21)$$

The unit of the equivalent strain is the square root of the unit of stress. It is also referred as “damage energy release rate” in the literature (Sáez et al., 2012). For the ground substance and the fibers in soft fibrous tissues, we assume that

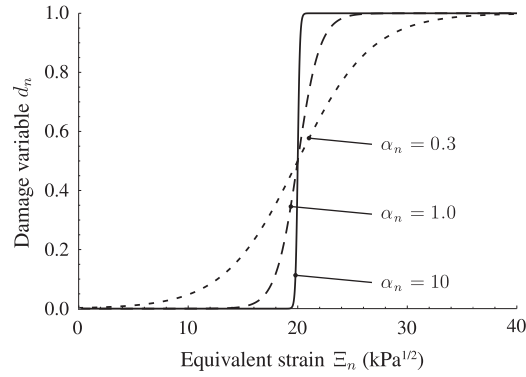


Fig. 2. Influence of parameter α_n on the fiber damage variable d_n according to (23)₂ while $\gamma_n = 20$.

there exists damage-initiation equivalent strains, Ξ_n^i or Ξ_n^i , at which damage initiates and maximum equivalent strains, Ξ_n^m or Ξ_n^m , at which complete material rupture occurs. Any deformation state prior to damage initiation incurs no damage in the tissue constituent, and the tissue constituent is purely elastic. Once damage initiates in any tissue constituent, either matrix or fiber, it becomes irreversible and permanent. This would affect the unloading and re-loading responses. Thus, tissue softening phenomena such as the Mullins effect only occurs at a certain stage of the loading history, not from the beginning of loading. Note that this is different from the preconditioning behavior of fibrous tissues because that is, in general, not damage induced. Once the equivalent strain in the ground substance or any fiber direction reaches a given maximum value, that constituent, either matrix or fiber, loses its load-bearing capacity permanently. The maximum equivalent strain here is a material property and does not evolve along the loading path (loading history), as in the model proposed for plastic deformation (Simo, 1987). Since the strain energy Ψ_n of a single fiber depends only on the true fiber stretch, the damage-initiation equivalent strain and the maximum equivalent strain of the collagen fibers can be described by the damage-initiation stretch λ_{di} and the maximum stretch λ_{max} , respectively, see Fig. 1. In this study, we assume both the damage-initiation and maximum equivalent strains are given (fixed) values, and both can be determined from experiments (Gentleman et al., 2003; Miyazaki and Hayashi, 1999; Pins et al., 1995). If a sudden rupture of a fiber is observed in the experiment (Pins et al., 1995), then the damage-initiation equivalent strain equals the maximum equivalent strain in this case. Since the maximum equivalent strain is a constant for the ground substance or fiber, we define the damage criterion in terms of the deformation as

$$\phi_g = \sqrt{2\Psi_g} - \Xi_g^m \leq 0, \quad \phi_n = \sqrt{2\Psi_n} - \Xi_n^m \leq 0, \quad n = 1, \dots, m. \quad (22)$$

The conditions $\phi_g = 0$ and $\phi_n = 0$ represent complete material damage. If $\phi_g < 0$ or $\phi_n < 0$, there may be some damage initiated in the tissue constituent. This depends on whether the equivalent strain in the tissue constituent reaches the threshold value or not.

To completely determine the constitutive model with damage, it remains to specify the functions of the damage variables. Those damage functions can be determined from experimental data of tissue constituents. There exists a number of damage functions in the literature (Holzapfel and Fereidoonzhad, 2017) for different types of materials. Following the suggestion in (Holzapfel and Fereidoonzhad, 2017), we adopt the damage function proposed in Peña (2011) for modeling the inelastic energy dissipation of the ground substance and fibers, i.e.

$$d_g(\Xi_g) = \frac{1}{1 + \exp[\alpha_g(\gamma_g - \Xi_g)]}, \quad (23)$$

$$d_n(\Xi_n) = \frac{1}{1 + \exp[\alpha_n(\gamma_n - \Xi_n)]}, \quad n = 1, \dots, m,$$

where α_g and γ_g are two constant damage parameters for the matrix material and α_n and γ_n are two constant damage parameters for the collagen fibers. Here we assume that the damage properties of the fibers are the same for all the fibers in the same family although it is allowed to assign a specific fiber damage property for any fiber direction. A representative example showing the effect of the parameter α_n on the fiber damage with a constant $\gamma_n = 20$ is plotted in Fig. 2. As shown, the parameter α_n controls the speed of the damage evolution and γ_n determines the value of Ξ_n such that $d_n(\Xi_n) = 0.5$. For convenience, now we write the reduction factor r_n of collagen fibers as

$$r_n(\Xi_n) = 1 - d_n(\Xi_n) = \frac{1}{1 + \exp[\alpha_n(\Xi_n - \gamma_n)]}, \quad n = 1, \dots, m, \quad (24)$$

and similarly for the matrix material, i.e.

$$r_g(\Xi_g) = 1 - d_g(\Xi_g) = \frac{1}{1 + \exp[\alpha_g(\Xi_g - \gamma_g)]}. \quad (25)$$

Thus, the isochoric strain-energy function (17) now becomes,

$$\Psi_{\text{iso}} = r_g \Psi_g + \sum_{n=1}^m \rho_n r_n \bar{\Psi}_n, \tag{26}$$

and, similarly, the isochoric second Piola–Kirchhoff stress tensor in (20)₃ now becomes

$$\mathbf{S}_{\text{iso}} = 2r_g \frac{\partial \Psi_g}{\partial \mathbf{C}} + 2 \sum_{n=1}^m \rho_n r_n \frac{\partial \bar{\Psi}_n}{\partial \mathbf{C}}. \tag{27}$$

2.5. Cauchy stress tensor

The fictitious second Piola–Kirchhoff stress tensor $\bar{\mathbf{S}}$ is required for the derivation of the Cauchy stress tensor. So we first differentiate the isochoric strain-energy function Ψ_{iso} in (26) with respect to $\bar{\mathbf{C}}/2$, similarly to (27), and obtain,

$$\begin{aligned} \bar{\mathbf{S}} &= 2 \frac{\partial \Psi_{\text{iso}}}{\partial \bar{\mathbf{C}}} = 2r_g \psi'_g(\bar{I}_1) \mathbf{I} + 2 \sum_{n=1}^m \rho_n r_n \bar{\mathbf{S}}_n, \\ \bar{\mathbf{S}}_n &= \frac{\partial \bar{\Psi}_n}{\partial \bar{\mathbf{C}}} = \begin{cases} \frac{1}{\lambda_r^2} f'(\bar{\lambda}_n^2) \mathbf{N}_n \otimes \mathbf{N}_n & \text{if } \lambda_n^2 \geq 1, \\ \mathbf{0} & \text{if } \lambda_n^2 < 1, \end{cases} \end{aligned} \tag{28}$$

where \mathbf{I} and $\mathbf{0}$ are the second-order unit and zero tensors, respectively, $\psi'_g(\bar{I}_1) = \partial \Psi_g(\bar{I}_1) / \partial \bar{I}_1$, and $f'(\bar{\lambda}_n^2) = \partial f(\bar{\lambda}_n^2) / \partial \bar{\lambda}_n^2$. If a different fiber recruitment stretch λ_r is required for each representative fiber orientation \mathbf{N}_n , then it should be replaced by λ_{rn} in (28)₄. Without loss of generality, we use a constant fiber recruitment stretch in this Section. Note that a variable fiber recruitment stretch is adopted in the third example in Section 4.

The fictitious Cauchy stress tensor $\bar{\boldsymbol{\sigma}}$ is then obtained by a push-forward operation of $\bar{\mathbf{S}}$ with $\bar{\mathbf{F}}$, i.e.

$$\begin{aligned} \bar{\boldsymbol{\sigma}} &= J^{-1} \bar{\mathbf{F}} \bar{\mathbf{S}} \bar{\mathbf{F}}^T = 2J^{-1} \left[r_g \psi'_g(\bar{I}_1) \bar{\mathbf{b}} + \sum_{n=1}^m \rho_n r_n \bar{\boldsymbol{\sigma}}_n \right], \\ \bar{\boldsymbol{\sigma}}_n &= \begin{cases} \frac{1}{\lambda_r^2} f'(\bar{\lambda}_n^2) \bar{\mathbf{n}}_n \otimes \bar{\mathbf{n}}_n & \text{if } \lambda_n^2 \geq 1, \\ \mathbf{0} & \text{if } \lambda_n^2 < 1, \end{cases} \end{aligned} \tag{29}$$

where $\bar{\mathbf{b}} = \bar{\mathbf{F}} \bar{\mathbf{F}}^T$ is the modified left Cauchy–Green tensor, and $\bar{\mathbf{n}}_n = \bar{\mathbf{F}} \mathbf{N}_n$. The isochoric Cauchy stress tensor $\boldsymbol{\sigma}_{\text{iso}}$ is then determined as

$$\boldsymbol{\sigma}_{\text{iso}} = \mathbb{P} : \bar{\boldsymbol{\sigma}}, \tag{30}$$

where $\mathbb{P} = \mathbb{I} - \frac{1}{3} \mathbf{I} \otimes \mathbf{I}$ is the fourth-order Eulerian projection tensor, and the symmetric fourth-order unit tensor \mathbb{I} is defined in component form by $(\mathbb{I})_{abcd} = \frac{1}{2} (\delta_{ac} \delta_{bd} + \delta_{ad} \delta_{bc})$, where δ_{ad} is the Kronecker delta.

2.6. Elasticity tensor

To determine the isochoric elasticity tensor, we begin with the derivation of the fourth-order fictitious elasticity tensor $\bar{\mathbb{C}}$ in the Lagrangian description. Thus, we differentiate $\bar{\mathbf{S}}$ in (28) with respect to $\bar{\mathbf{C}}/2$ and multiply by a factor of $J^{-4/3}$, i.e.

$$\begin{aligned} \bar{\mathbb{C}} &= 2J^{-4/3} \frac{\partial \bar{\mathbf{S}}}{\partial \bar{\mathbf{C}}} = 4J^{-4/3} r_g \psi''_g(\bar{I}_1) \mathbf{I} \otimes \mathbf{I} + 4J^{-4/3} \sum_{n=1}^m \rho_n r_n \bar{\mathbb{C}}_n, \\ \bar{\mathbb{C}}_n &= \frac{\partial \bar{\mathbf{S}}_n}{\partial \bar{\mathbf{C}}} = \begin{cases} \frac{1}{\lambda_r^4} f''(\bar{\lambda}_n^2) \mathbf{N}_n \otimes \mathbf{N}_n \otimes \mathbf{N}_n \otimes \mathbf{N}_n & \text{if } \lambda_n^2 \geq 1, \\ \mathbb{0} & \text{if } \lambda_n^2 < 1, \end{cases} \end{aligned} \tag{31}$$

where $\mathbb{0}$ denotes the fourth-order zero tensor in the Lagrangian description and

$$\psi''_g(\bar{I}_1) = \frac{\partial^2 \Psi_g(\bar{I}_1)}{\partial \bar{I}_1 \partial \bar{I}_1}, \quad f''(\bar{\lambda}_n^2) = \frac{\partial^2 f(\bar{\lambda}_n^2)}{\partial \bar{\lambda}_n^2 \partial \bar{\lambda}_n^2}. \tag{32}$$

Then, a push-forward operation of $\bar{\mathbb{C}}$ with \mathbf{F} yields the fictitious elasticity tensor in the Eulerian description, i.e.

$$\bar{\mathbb{C}} = 4J^{-1} \sum_{n=1}^m \rho_n r_n \bar{\mathbb{C}}_n, \quad \bar{\mathbb{C}}_n = \begin{cases} \frac{1}{\lambda_r^4} f''(\bar{\lambda}_n^2) \bar{\mathbf{n}}_n \otimes \bar{\mathbf{n}}_n \otimes \bar{\mathbf{n}}_n \otimes \bar{\mathbf{n}}_n & \text{if } \lambda_n^2 \geq 1, \\ \mathbb{0} & \text{if } \lambda_n^2 < 1, \end{cases} \tag{33}$$

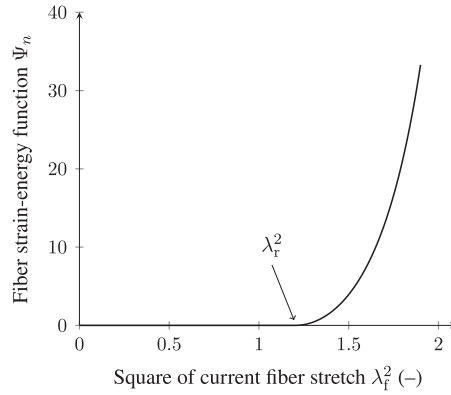


Fig. 3. An example plot of a strain-energy function Ψ_n obtained by substituting (9) and (36) into (11) associated with one fiber direction versus square of current fiber stretch λ_f^2 . Note that Ψ_n becomes positive when the true fiber stretch is greater than one ($\lambda_f > \lambda_r$) and the transition of the curve from the wavy state of fiber to the stressed state is smooth. No fiber damage is considered in this plot.

where $\mathbb{0}$ denotes the fourth-order zero tensor in the Eulerian description, and we have used the neo-Hookean model (15) so that $\psi_g''(\bar{I}_1) = 0$. If $\psi_g''(\bar{I}_1) \neq 0$, then an additional term should be included in (33)₁. Finally, with (33), we obtain the resulting isochoric part of the elasticity tensor in the Eulerian description, i.e.

$$\mathbb{C}_{\text{iso}} = \mathbb{P} : \bar{\mathbb{C}} : \mathbb{P} + \frac{2}{3} \text{tr}(\bar{\boldsymbol{\sigma}})_{\mathbb{P}} - \frac{2}{3} (\boldsymbol{\sigma}_{\text{iso}} \otimes \mathbf{I} + \mathbf{I} \otimes \boldsymbol{\sigma}_{\text{iso}}), \tag{34}$$

which is needed for the finite element implementation together with the volumetric part (Holzapfel, 2000).

3. Computational aspects and implementation

We have implemented the proposed constitutive model with fiber recruitment and damage (17) in the general purpose finite element analysis program FEAP (Taylor, 2013) at the integration point level. The damage variables are stored as history variables for the computation of the Cauchy stress and elasticity tensors at each integration point.

3.1. Fiber distribution function

Since our constitutive formulation in Section 2 is independent of the fiber PDF $\rho(\Theta, \Phi)$, our model is applicable to any type of fiber distribution, symmetric or non-symmetric. It is also possible to modify our formulation for two-dimensional planar fiber distributions. Here, we confine our attention to the 3D fiber distribution and adopt the rotationally symmetric fiber dispersion described by the von Mises distribution for fiber PDF

$$\rho(\Theta, \Phi) = 4 \sqrt{\frac{b}{2\pi}} \frac{\exp[2b(\mathbf{N} \cdot \mathbf{M})^2]}{\text{erfi}(\sqrt{2b})}, \tag{35}$$

where b is a concentration parameter describing how closely the fibers are distributed around the mean fiber direction \mathbf{M} within a family, $\text{erfi}(x) = -i \text{erf}(ix)$ denotes the imaginary error function. This distribution will be used in all the numerical examples. On substituting (35) into (6), we obtain a set of m elementary fiber densities ρ_n for the representative fiber directions \mathbf{N}_n , $n = 1, \dots, m$.

3.2. Fiber strain-energy function

Our constitutive formulation is not restricted to any particular form of the single fiber strain-energy function $f(\lambda_n^2)$. Again, this function should be chosen according to the experimental data of the specific fiber in the fibrous tissue. As discussed in Section 1, we choose an exponential strain-energy function, as proposed in Holzapfel et al. (2000), for illustration of the method, i.e.

$$f(\lambda_n^2) = \frac{k_1}{2k_2} \{ \exp[k_2(\lambda_n^2 - 1)^2] - 1 \}, \tag{36}$$

where k_1 is a positive material parameter with the dimension of stress, and k_2 is a positive dimensionless parameter. It is easy to verify that (36) satisfies $f(1) = f'(1) = 0$, $f(\lambda_n^2) > 0$ and $f'(\lambda_n^2) > 0$ for $\lambda_n^2 > 1$, and hence, requirement (5) is also satisfied. A representative plot of the strain-energy function Ψ_n associated with one fiber direction versus the square of current fiber stretch λ_f^2 is shown in Fig. 3. As can be seen, the strain energy is only non-zero when the true fiber stretch is greater than one or $\lambda_f > \lambda_r$. Note that the first derivative of the strain-energy function with respect to λ_f^2 is continuous

and equal to zero at $\lambda_f = \lambda_r$. On substituting (36) into the isochoric Cauchy stress tensor (29) and the Eulerian fictitious elasticity tensor (33) with λ_n^2 replaced by its isochoric counterpart $\bar{\lambda}_n^2$, we obtain the specific forms of the Cauchy stress and Eulerian elasticity tensors.

4. Representative examples

In this section, the procedure to determinate the material, structural and damage parameters in the constitutive model is first described. Some parameters are approximated based on the published experimental data. Then, we present three numerical examples to illustrate the performance of the proposed constitutive law in modeling the fiber recruitment, softening and damage, specifically the homogeneous simple tension and simple shear of a unit cube with a 3D fiber dispersion, and an inhomogeneous uniaxial extension test of a dog-bone shaped specimen with two fiber families identified from image analysis of the actual specimen. Due to the lack of experimental data on the damage of the non-collagenous matrix material, the damage of the matrix material is not accounted for in all the numerical examples. Only fiber damage is considered. We assume incompressible material in all the examples. The augmented Lagrangian method (Simo and Taylor, 1991) in FEAP is used to enforce the incompressibility condition with a penalty parameter of $K = 1.0 \times 10^7$ kPa in all the examples. In each example, the geometry of the model is discretized with 8–node hexahedral mixed Q1/P0 elements, and each problem is solved by using the Newton–Raphson method in FEAP. The goal of this section is not to simulate the post-failure tissue separation observed in the experiment because that poses challenging convergence problems (Sáez et al., 2012) and requires special numerical methods such as the combined particle/continuum approach recently proposed (Rausch et al., 2017) or the element deletion method in Abaqus (Dassault Systèmes 2017a). The finite element solutions of the three examples are then compared with either theoretical solutions or experimental data.

4.1. Determination of constitutive parameters

Because of the multiscale nature of our constitutive model, the corresponding constitutive parameters should also be determined from data at different scales. In this study, for illustration of the method, we determined the material and structural parameters according to the uniaxial extension test results of a medial layer from a human thoracic aorta at our laboratory and mechanical responses of collagen fibers from the literature. The experimental protocol of the uniaxial extension test has been previously described (Weisbecker et al., 2013). Briefly, the media layer of the human thoracic aorta from a 65-year-old female patient with lung cancer and high blood pressure, who passed away due to tumor progression, was first separated from the surrounding tissues and then cut into a dog-bone shaped specimen with a metal template. Two black markers were affixed to the central region of the specimen for displacement measurements. The specimen was then preconditioned and subjected to uniaxial extension test up to failure. All tests were carried out in a physiological bath at 37 °C. Displacement of markers and driven force data were recorded simultaneously. Cauchy stress versus stretch curve was then computed and plotted, and the 3D fiber dispersion within the specimen was investigated by using SHG (Schriebl et al., 2012) after the experiment. Through image analyses, we identified two fiber families within this specimen, and the fitting of the image data with the von Mises distribution function (35) indicated an averaged concentration parameter of $b = 1.435$ for both fiber families.

From the initial slope of the Cauchy stress versus stretch curve in the linear range, we can approximate the shear modulus of the matrix material to be $\mu = 47.41$ kPa, which is similar to our previously measured values of the non-collagenous matrix material from the medial layer of human thoracic aorta (Weisbecker et al., 2013). Ideally, the fiber recruitment stretch should be determined from image analyses of the fiber morphology in the specimen. However, due to the lack of these data, we approximated the fiber recruitment stretch λ_r from the stress versus stretch curve by determining the location at which the slope of the curve starts to increase. According to the extensive image analyses of the fiber uncrimping process in rabbit carotid arteries under uniaxial extension tests (Hill et al., 2012), the fiber recruitment apparently occurs right before the transition region of the stress versus stretch curve. The specific point where the slope changes is the location at which the fibers start to contribute to the strain-energy function. We then determined a recruitment stretch between 1.34 and 1.43 for this specimen. We use a constant value for all fiber directions throughout the specimen in the first two examples. In the third example, we use a varying fiber recruitment stretch within the determined range.

To identify the damage parameters in the reduction factor and the material parameters of the fiber in the strain-energy function, we treat the collagen fibers as string-like, crimped, and also incompressible structures in the reference configuration. After straightened under axial loading, the Cauchy stress σ_f in any fiber direction is obtained (Holzapfel, 2000) via (36) as

$$\sigma_f = 2\lambda_n^2 r_n \frac{\partial f(\lambda_n^2)}{\partial \lambda_n^2} = 2k_1 r_n \lambda_n^2 (\lambda_n^2 - 1) \exp[k_2 (\lambda_n^2 - 1)^2], \tag{37}$$

where r_n is now

$$r_n = \frac{1}{1 + \exp[\alpha(\sqrt{2f} - \gamma)]}. \tag{38}$$

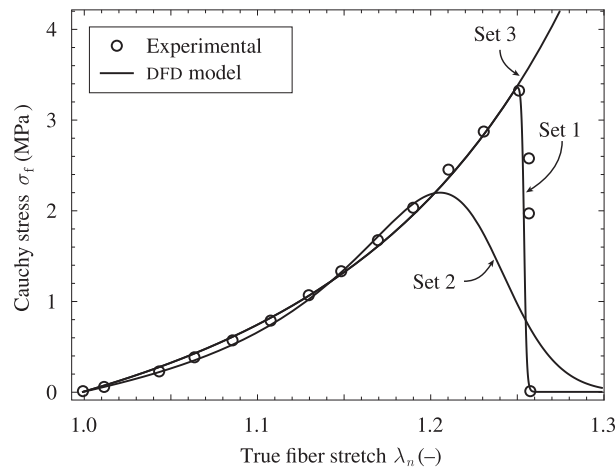


Fig. 4. Determination of the fiber parameters (k_1 , k_2 , α , and γ) in the proposed discrete fiber dispersion (DFD) model according to the experimental data (Enea et al., 2011) of the stress versus the true fiber stretch curve. The experimental test was performed from the straightened state of the fiber, see Fig. 1. Parameter sets 2 and 3 are created for comparison.

Table 1

Constitutive parameters obtained from experimental and imaging data of the human aortic specimen together with fiber parameters (k_1 , k_2 , α , and γ) determined according to the experimental data (Enea et al., 2011).

Parameter	μ (kPa)	b	k_1 (MPa)	k_2	λ_r	α	γ (Pa)
Set 1			1.38	1.02	1	0.35	735.5
Set 2	47.41	1.435	1.08	4.1	1.35	0.01	658.5
Set 3			1.38	1.02	1	–	–

Since we assume that the fibers in the same family have the same mechanical properties, the damage parameters α and γ for the fibers are constants. Due to the limited experimental data on the mechanical response and failure behavior of collagen fibers, in this study, we approximate the mechanical and failure properties of collagen fiber by using the failure testing results of cross-linked fibers in Enea et al. (2011). We fitted the analytical solution (37) with the experimental data in Mathematica and obtained a set of parameters. To demonstrate the capability of the proposed constitutive law in modeling both fiber softening and damage, we created a second set of parameters, see Fig. 4. As the damage parameter α is reduced, the damage evolution is much slower in the second case. A third set of parameters was also created for comparing with the case of no fiber damage and uncrimping. To eliminate fiber damage in the third case, we set the reduction factor $r_n \equiv 1$ in all fiber directions. The three sets of parameters are summarized in Table 1, which are used in the numerical examples. In the third example, the mechanical parameters of the fibers are further adjusted in order to simulate the actual human tissue behavior.

4.2. Fiber recruitment and damage under simple tension

In this example, we examine the effects of fiber recruitment and damage on the tissue responses undergoing uniaxial tension. The tissue is modeled as an incompressible unit cube described previously (Li et al., 2018a; 2018b). Briefly, we consider an isotropic matrix material in which one family of fibers is embedded. The mean fiber direction \mathbf{M} is aligned with the loading direction \mathbf{E}_3 . We assume a rotationally symmetric dispersion of fibers around the mean direction, see a cross section of the fiber distribution in Fig. 5. A displacement boundary condition is then imposed on the top face of the cube up to a stretch of 1.75, see Fig. 5. As discussed in our previous study (Holzapfel and Ogden, 2017), only a subset of fibers around the mean fiber direction within the dispersion and the mean fiber direction itself are under tension when the cube is loaded, and the rest of the fibers are under compression. The fibers straightened (recruited) and stretched first will also damage first. However, with the increase of deformation, more and more fibers become recruited and start to contribute to the total strain energy. Thus, there may be a second smaller peak stress after the first one in the stress versus stretch curve. This kind of post-damage material behavior depends on the underlying microscopic fiber morphology.

For this particular example, the squared fiber stretch $I_4(\mathbf{N})$ in the fiber direction \mathbf{N} is given by

$$I_4(\mathbf{N}) = \lambda^{-1} \sin^2 \Theta + \lambda^2 \cos^2 \Theta, \quad (39)$$

where λ is determined by the applied displacement in the loading direction, and Θ is the angle between \mathbf{N} and the mean fiber direction, see Fig. 5. Note that $I_4(\mathbf{N})$ is independent of Φ in this special case. For a verification of the computational

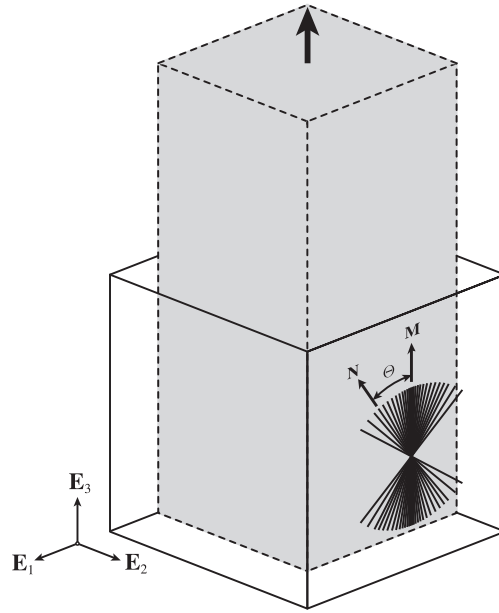


Fig. 5. Deformation of a unit cube under simple tension. We assume a rotationally symmetric fiber dispersion with the mean fiber direction \mathbf{M} aligned along the loading direction \mathbf{E}_3 in the reference configuration (solid lines). An arbitrary fiber direction within the dispersion is denoted by \mathbf{N} . The fiber dispersion is 3D but only a cross-section in the $(\mathbf{E}_1, \mathbf{E}_3)$ -plane is shown. The dashed lines refer to the deformed configuration of the cube, shown in grey, at a stretch of 1.75.

solution, the theoretical solution of the Cauchy stress in the loading direction needs to be determined. We start with the strain–energy function of the CFD model described in Li et al. (2018b) and consider only the fiber damage, i.e.

$$\Psi = \Psi_g(I_1) + \frac{1}{2\pi} \int_{\Omega} \rho(\Theta, \Phi) r_n \Psi_n(\lambda_n^2) \sin \Theta d\Theta d\Phi, \tag{40}$$

where the integration domain is now $\Omega = \{(\Theta, \Phi) \mid \Theta \in [0, \pi/2], \Phi \in [0, 2\pi], I_4 > \lambda_r^2\}$. Within this domain, the fiber strain energy $\Psi_n(\lambda_n^2) > 0$. Following the same procedure as in Section 2, we obtain the general form of the Cauchy stress tensor σ , i.e.

$$\sigma = -p\mathbf{I} + \mu\mathbf{b} + \frac{k_1}{\pi\lambda_r^2} \int_{\Omega} \rho(\Theta, \Phi) r_n \exp[k_2(\lambda_n^2 - 1)^2](\lambda_n^2 - 1) \sin \Theta \mathbf{n} \otimes \mathbf{n} d\Theta d\Phi, \tag{41}$$

where we have used the neo-Hookean model for the matrix material and replaced $\Psi_n(\lambda_n^2)$ by $f(\lambda_n^2)$ in (36), p is the Lagrange multiplier, $\mathbf{n} = \mathbf{F}\mathbf{N}$, and, because of symmetry in this particular example, the PDF $\rho(\Theta, \Phi)$ reduces to

$$\rho(\Theta) = 4\sqrt{\frac{b}{2\pi}} \frac{\exp(2b \cos^2 \Theta)}{\operatorname{erfi}(\sqrt{2b})}. \tag{42}$$

Similarly to the stress solution in Li et al. (2018b), the Cauchy stress component σ_{33} in the loading direction \mathbf{E}_3 is

$$\sigma_{33} = (\mu + \delta)\lambda^2 - (\mu + \beta)\lambda^{-1}, \tag{43}$$

where δ and β are defined over the domain $\Sigma = \{\Theta \in [0, \pi/2] \mid I_4 > \lambda_r^2\}$ as

$$\begin{aligned} \delta &= \frac{2k_1}{\lambda_r^2} \int_{\Sigma} \rho(\Theta) r_n \exp[k_2(\lambda_n^2 - 1)^2](\lambda_n^2 - 1) \sin \Theta \cos^2 \Theta d\Theta, \\ \beta &= \frac{k_1}{\lambda_r^2} \int_{\Sigma} \rho(\Theta) r_n \exp[k_2(\lambda_n^2 - 1)^2](\lambda_n^2 - 1) \sin^3 \Theta d\Theta. \end{aligned} \tag{44}$$

We implemented the theoretical result of the Cauchy stress (43) in MATLAB and obtained the solution of this example with three sets of the constitutive parameters listed Table 1. The theoretical and computational solutions of the Cauchy stress versus stretch are plotted in Fig. 6 with different fiber recruitment and damage parameters. Firstly, we study the Cauchy stress response of the unit cube with fiber damage but without fiber uncrimping ($\lambda_r \equiv 1$) by using the parameter set 1. Because fiber rupture occurs right after damage initiation, see the fiber stress versus stretch curve with parameter set 1 in Fig. 4, the Cauchy stress decreases abruptly after reaching the peak value. This type of abrupt tissue failure has also been observed in experimental studies, see, for example, the recent study (Sang et al., 2018).

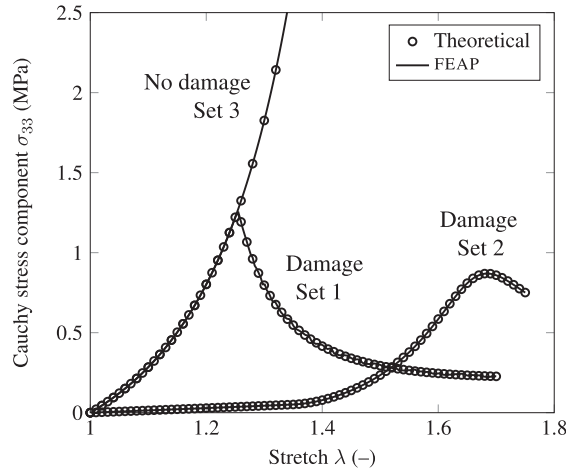


Fig. 6. Comparison of the theoretical solutions obtained by using the CFD model (Li et al., 2018b) in MATLAB with the computational solutions obtained by using the proposed DFD model with $m = 4000$ of a unit cube under simple tension test. The three sets of material parameters used in the calculation of both the theoretical and computational solutions are listed in Table 1.

In addition, a gradual tissue failure has also been observed in many experimental studies (Sang et al., 2018; Zuo et al., 2016). To demonstrate the capability of the proposed constitutive law for modeling tissue softening and gradual failure, we adjusted the fiber damage parameters and plotted the Cauchy stress results corresponding to the parameter set 2 in Fig. 6. A constant fiber recruitment stretch of $r_n = 1.35$ was applied for all the fiber directions in the model. As shown, the Cauchy stress increases linearly in the beginning and then rises rapidly once the fibers start to recruit. Note that the fiber recruitment occurs in the region near the mean fiber direction first and then expands to a large domain until tissue failure. Due to this gradual fiber recruitment and fiber softening, the tissue experiences softening, and then the Cauchy stress decreases gradually after reaching the peak value.

Finally, for comparison purposes we have also plotted the result without damage and uncrimping corresponding to parameter set 3. In this case, the reduction factor is $r_n \equiv 1$ and $\lambda_r = 1$. Thus, the fibers start to contribute to the total strain energy immediately and show no softening and damage. As shown in Fig. 6, we obtained a very good agreement between the theoretical solutions obtained by using (43) and the finite element solutions with $m = 4000$ for all three cases. This indicates that the proposed DFD model is able to predict the same result as the CFD model for human aortic tissue under simple tension.

4.3. Fiber recruitment and damage under simple shear

In the previous section we demonstrated the capability of the proposed DFD model under simple tension, in this second example we investigate the effects of fiber recruitment and damage on the mechanical responses of the same unit cube under simple shear. Details of the simple shear model have been previously described (Li et al., 2018a; 2018b). Briefly, all the nodes on the bottom face of the cube in the $(\mathbf{E}_1, \mathbf{E}_2)$ -plane are constrained in all three translational degrees of freedom, and a horizontal displacement in the \mathbf{E}_1 direction is applied on the top face, see Fig. 7. Previously, we have aligned the mean fiber direction 135° clockwise from the \mathbf{E}_3 direction so that the exclusion of fibers under compression has a significant influence on the resulting shear stress. However, in order to demonstrate the tissue softening and damage at an earlier stage, in this study, we align the mean fiber direction \mathbf{M} to be at 45° clockwise from the \mathbf{E}_3 direction in the $(\mathbf{E}_1, \mathbf{E}_3)$ -plane of the reference configuration, as illustrated on a cross-section of the cube in Fig. 7. Thus, the fibers in this example are primarily under tension. We have also increased the amount of shear c applied on the top face of the cube so that both damage initiation and evolution occur in the simulation.

The theoretical solution (Li et al., 2018b) of the Cauchy shear stress component σ_{13} in the $(\mathbf{E}_1, \mathbf{E}_3)$ -plane can be deduced from the general form of Cauchy stress tensor (41), i.e.

$$\sigma_{13} = (\mu + \delta)c + \eta, \quad (45)$$

where δ and η are defined by

$$\begin{aligned} \delta &= \frac{k_1}{\pi \lambda_f^2} \int_{\Omega} \rho(\Theta, \Phi) r_n (\lambda_n^2 - 1) \exp[k_2 (\lambda_n^2 - 1)^2] \sin \Theta \cos^2 \Theta d\Theta d\Phi, \\ \eta &= \frac{k_1}{\pi \lambda_f^2} \int_{\Omega} \rho(\Theta, \Phi) r_n (\lambda_n^2 - 1) \exp[k_2 (\lambda_n^2 - 1)^2] \sin^2 \Theta \cos \Theta \cos \Phi d\Theta d\Phi, \end{aligned} \quad (46)$$

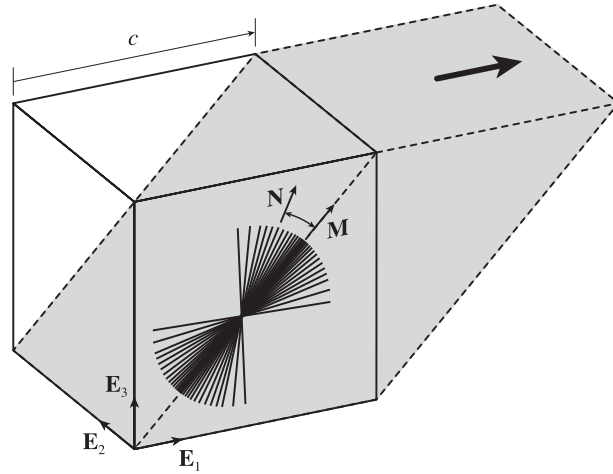


Fig. 7. Simulation of fiber recruitment and damage by using a unit cube under simple shear in the $(\mathbf{E}_1, \mathbf{E}_3)$ -plane. The mean fiber direction \mathbf{M} is aligned at 45° clockwise from the \mathbf{E}_3 direction in the reference configuration (solid lines). The 3D fiber dispersion is rotationally symmetric about \mathbf{M} , although only a cross-section in the $(\mathbf{E}_1, \mathbf{E}_3)$ -plane is shown. The unit vector \mathbf{N} in that cross-section represents a general fiber direction. The dashed lines refer to the deformed configuration of the cube, shown in grey, with an amount of shear $c = 1.0$.

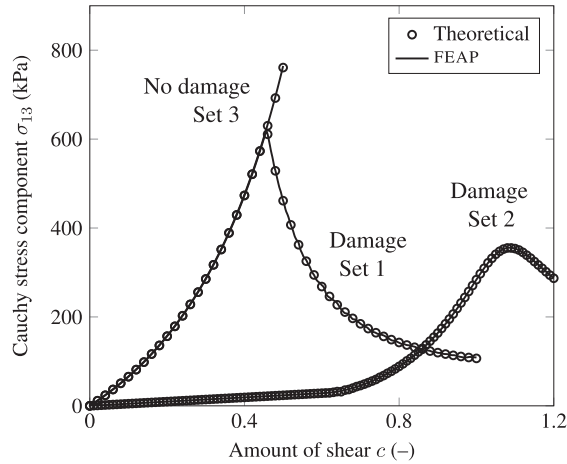


Fig. 8. Comparison of the theoretical solutions obtained by using the CFD model (Li et al., 2018b) and Mathematica with the finite element solutions obtained by the proposed DFD model with $m = 4000$ for a simple shear test of a unit cube. The three sets of material parameters used in the calculation of both the theoretical and computational solutions are listed in Table 1.

and $\Omega = \{(\Theta, \Phi) \in \mathbb{S} \mid I_4 > \lambda_r^2\}$. For this particular example, the invariant $I_4(\mathbf{N})$ has the explicit form (Li et al., 2016)

$$I_4(\Theta, \Phi) = 1 + c^2 \cos^2 \Theta + c \sin 2\Theta \cos \Phi. \tag{47}$$

Thus, the integration boundary for excluding the fibers under compression now becomes

$$c \cos^2 \Theta + \sin 2\Theta \cos \Phi > (\lambda_r^2 - 1)/c. \tag{48}$$

We implemented the Cauchy shear stress result (45) with the integration boundary (48) in Mathematica and obtained the theoretical solutions of this problem with three sets of constitutive parameters listed in Table 1. Firstly, we investigated the shear stress response of the unit cube with fiber damage but no fiber uncrimping by using parameter set 1. Similarly to the uniaxial tension test, the shear stress increases first and then reduces sharply after the peak value due to the specific type of fiber damage definition. In addition, a gradual tissue failure has also been observed in shear tests (Sommer et al., 2016). We then plotted the shear stress result corresponding to parameter set 2. In this second case, we observed a very similar stress response to the uniaxial test. The shear stress increases linearly in the beginning and then rises rapidly once the fibers start to recruit. For comparison, we have also plotted the case without fiber damage and fiber uncrimping by using parameter set 3, see Fig. 8. In this third case, the shear stress increases monotonically with respect to the amount of shear. As can be seen, the computational results (solid curves) match very well with the corresponding theoretical solutions (open circles) obtained by using (45) in Mathematica for all three cases. This confirms that our proposed DFD model is able to capture the tissue softening and damage under simple shear deformation as well.

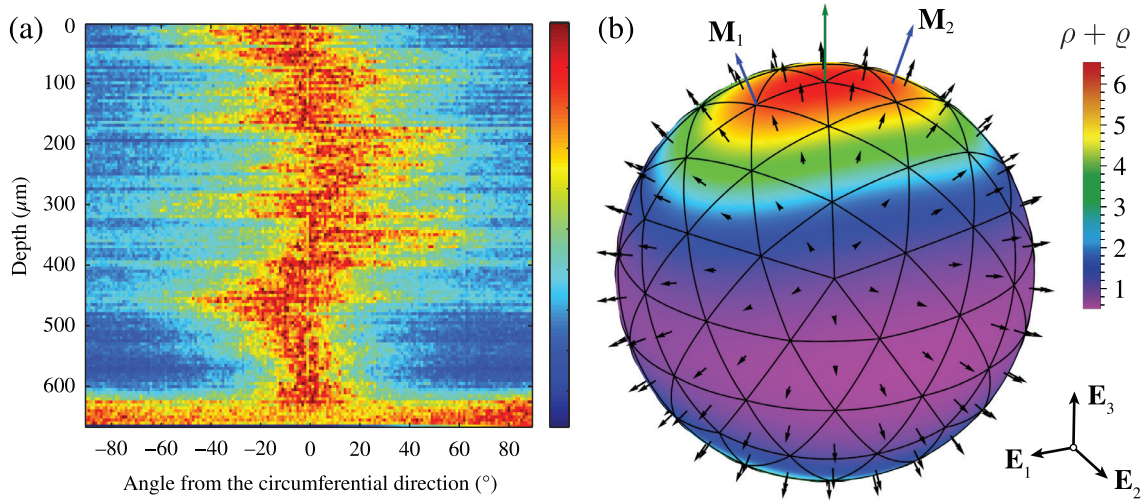


Fig. 9. Determination and modeling of 3D fiber dispersion. (a) intensity plot (non-smoothed) illustrating the variation of the collagen fiber directions through the medial layer where dark blue color indicates less fibers and dark red color indicates dense fibers on the color bar, and 0° on the horizontal axis indicates the circumferential direction of the specimen; (b) fitting result of the fiber intensity data in (a) with two families of rotationally symmetric fiber dispersion functions. The green arrow indicates the circumferential direction of the specimen, and the blue arrows indicate the mean fiber directions of the two fiber families ($\pm 19.76^\circ$ from the circumferential direction). (For interpretation of the references to colour in this figure legend, the reader is referred to the web version of this article.)

4.4. Simulation of a uniaxial failure test

Since the most common failure test performed on soft biological tissues is the uniaxial extension test, in this example, we study the effects of fiber recruitment and damage on the mechanical responses of arterial tissue until failure. Specifically, we consider the uniaxial extension test on a dog-bone shaped medial layer specimen of human thoracic aorta with loading in the circumferential direction. The computational analyses of this problem are performed according to the experimental condition and protocol which has been briefly described in Section 4.1. For this problem the deformation field is non-homogeneous, as distinct from the previous two examples.

The geometry and boundary conditions of the finite element model are defined according to the actual specimen used in the experiment and experimental conditions, respectively. Briefly, the geometry of the finite element model was created by using the geometry of the metal template and the image of the specimen before testing. It is 17 mm long, 1.1 mm thick, and 4 mm wide in the central region. The geometrical model of the dog-bone shaped specimen is then discretized with 4032 hexahedral elements in Abaqus/CAE 2017 (Dassault Systèmes, 2017a) and converted into the FEAP input file format. Similarly to the experimental conditions, all the nodes on the bottom face of the model are constrained in all three directions. In addition, a displacement boundary condition is applied on the top face of the model to impose a stretch in the \mathbf{E}_3 direction up to failure. The \mathbf{E}_1 and \mathbf{E}_2 degrees of freedom at all the nodes on the top face of the model are also constrained, see Fig. 11(a).

After the experiment, the specimen was further analyzed by using SHC for the quantification of the fiber orientations through the thickness of the specimen, and from the non-smoothed intensity plot of the specimen, see Fig. 9(a), we identified two families of fibers with the mean directions $\pm 19.76^\circ$ from the circumferential direction on the tangential plane of the arterial wall. The averaged concentration parameter for both fiber families was estimated to be $b = 1.435$. Thus, we write the two fiber PDFs as

$$\rho(\Theta, \Phi) = 4\sqrt{\frac{b}{2\pi}} \frac{\exp[2b(\mathbf{N} \cdot \mathbf{M}_1)^2]}{\operatorname{erfi}(\sqrt{2b})}, \quad \varrho(\Theta, \Phi) = 4\sqrt{\frac{b}{2\pi}} \frac{\exp[2b(\mathbf{N} \cdot \mathbf{M}_2)^2]}{\operatorname{erfi}(\sqrt{2b})}, \quad (49)$$

where $\mathbf{M}_1 = \sin(19.76^\circ)\mathbf{E}_1 + \cos(19.76^\circ)\mathbf{E}_3$ and $\mathbf{M}_2 = \sin(-19.76^\circ)\mathbf{E}_1 + \cos(-19.76^\circ)\mathbf{E}_3$ represent the mean fiber directions of the two fiber families, see the blue arrows in Fig. 9(b). They are fixed vectors given in the reference configuration. Superposition of the two fiber PDFs $\rho(\Theta, \Phi)$ and $\varrho(\Theta, \Phi)$ yields the final fiber distribution over the unit sphere as shown in Fig. 9(b). Through triangular discretization of the superimposed fiber density functions over the unit sphere, we obtained one set of elementary fiber densities for both fiber families by numerical integration of the sum of $\rho(\Theta, \Phi)$ and $\varrho(\Theta, \Phi)$ over each elementary area (8). For the calculation of the fiber strain energy at each representative fiber direction, the fiber recruitment stretch λ_f remains to be determined. Because the actual fiber waviness is varying and we estimated the range of the fiber recruitment stretch from the stress versus stretch curve in Section 4.1 to be between 1.34 and 1.43, we assigned a random number between 1.34 and 1.43 to the fiber recruitment stretch for each representative fiber direction over the hemisphere. Each representative fiber orientation at any Gauss point will be assigned with the same random number. Those

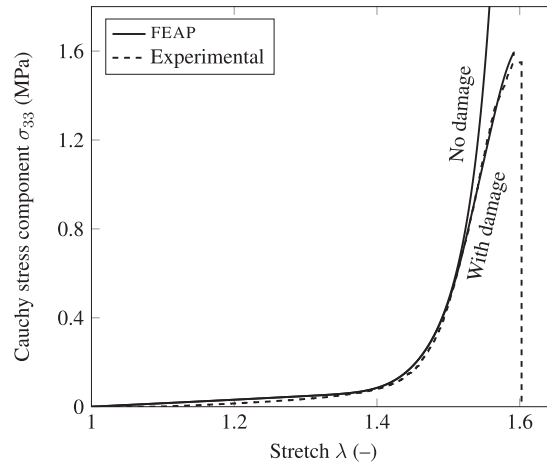


Fig. 10. Comparison of the experimental data (dashed curve) with the computational solutions (solid curves) obtained by using the proposed bFD model for the uniaxial test on the medial layer of a human thoracic aorta up to failure. The material, structural, and damage parameters used in the computational model are listed in Table 2. For comparison, the computational solution for the case without damage ($r_n \equiv 1$) is also plotted.

Table 2

Constitutive parameters obtained from experimental and imaging data of the aortic specimen together with fiber parameters (k_1 , k_2 , α , and γ) identified according to the experimental data (Enea et al., 2011) for the uniaxial failure simulation of a human thoracic aorta (medial layer only).

Parameter	μ (kPa)	b	k_1 (MPa)	k_2	λ_r	α	γ (Pa)
Set 4	47.41	1.435	1.43	22.8	1.34 ~ 1.43	0.011	680.5

random fiber recruitment stretch and elementary fiber density associated with each representative fiber orientation are then used in the computation of the stress and elasticity tensors.

The Cauchy stress versus stretch curve obtained from the experiment is plotted in Fig. 10 (dashed curves). As shown, the tissue softening occurred before the final rupture. To simulate the softening response of this specimen with the proposed constitutive model, we have adjusted the fiber parameters because the actual fiber properties are unknown. Through trial and error, we obtained a fourth set of parameters listed in Table 2. The computational result of the averaged Cauchy stress component σ_{33} over the central elements (marked red in Fig. 11(a)) versus the total stretch with this set of fiber parameters is plotted in Fig. 10. As shown, we have obtained a good agreement between the experimental and computational results. Note that the experimental result was also measured over the central region of the specimen with two black markers. Thus, we only extracted the stress output from the central elements of the model for comparison. The contour plots of the Cauchy stress component σ_{33} at different loading steps during the simulation are shown in Fig. 11. It is clear that both the thickness and width of the model reduce gradually with the increase of the displacement in the E_3 direction. Note that the trial and error process for the determination of an optimal set of fiber parameters could also be performed automatically by using a process automation and design optimization program, for example, Simulia Isight (Li and Sun, 2017; Dassault Systèmes, 2017b). For comparison, we also performed the uniaxial extension simulation of the dog-bone shaped specimen without fiber damage. As shown in Fig. 10, the averaged Cauchy stress over the central elements versus the stretch deviates from the experimental result after damage initiation in the fibers.

To further investigate the effect of fiber damage on the mechanical response of arterial tissue, we performed a simulation of cyclic loading on the dog-bone shaped specimen. Firstly, we increased the displacement to a stretch of 1.5 and then unloaded the specimen. Secondly, we reloaded the specimen to a stretch of 1.56 and unloaded it again. Finally, we loaded the specimen up to failure. The averaged Cauchy stress component σ_{33} over the central elements (marked red in Fig. 11(a)) versus the total stretch λ is shown in Fig. 12(a). The normalized displacement applied on the top face of the model versus the time step is shown in Fig. 12(b). As shown in Fig. 12(a), the first unloading curve is almost identical to the primary loading curve due to the negligible damage accumulated in the fibers. However, the second unloading curve is clearly distinguishable from the primary loading curve. Due to the non-homogeneous deformation during the cyclic loading process, the damage evolution should also be non-homogeneous. To confirm the non-homogeneous damage evolution, we also plotted the reduction factor of the fiber aligned in the circumferential direction (identical to the loading direction) versus the time step for two different elements of the computational model in Fig. 12(b), namely element A and element B in Fig. 11(a). As can be seen, the damage initiated first in element B then in element A. In addition, the damage progressed faster in element B than in element A towards the end of the simulation. Furthermore, damage evolution only occurs on the primary loading curve of the Cauchy stress versus the total stretch plot, see Fig. 12(a).

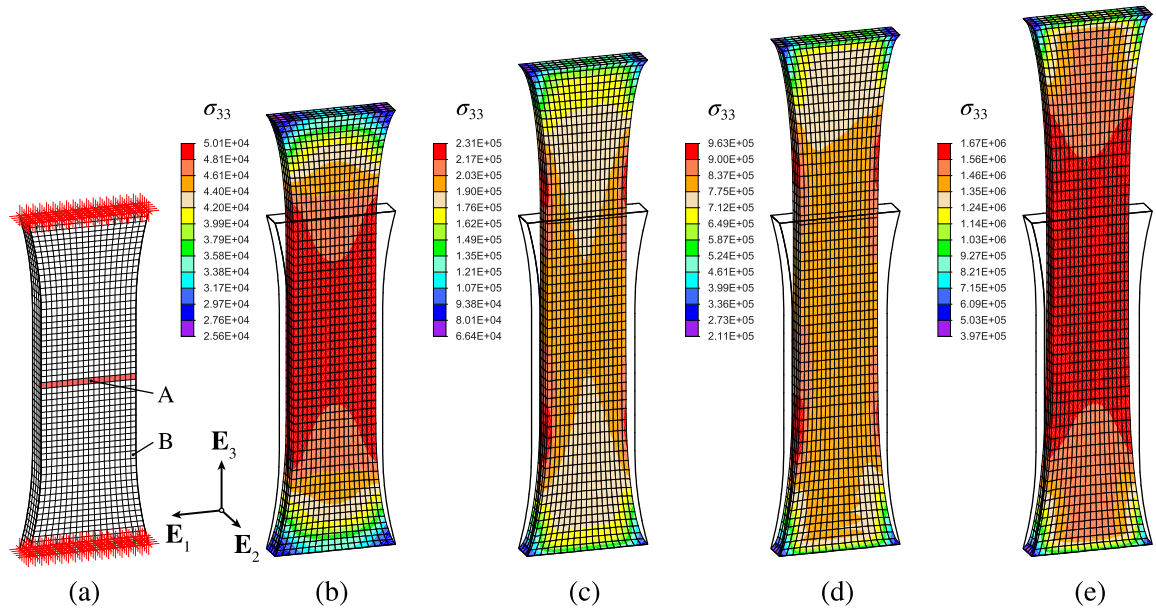


Fig. 11. Finite element model (a) and distribution of Cauchy stress component σ_{33} (Pa) for a dog-bone shaped specimen at different loading steps: (b) $\lambda = 1.3$, (c) $\lambda = 1.45$, (d) $\lambda = 1.53$, and (e) $\lambda = 1.59$. The material and damage parameters used in the computational model are listed in Table 2. (For interpretation of the references to colour in this figure legend, the reader is referred to the web version of this article.)

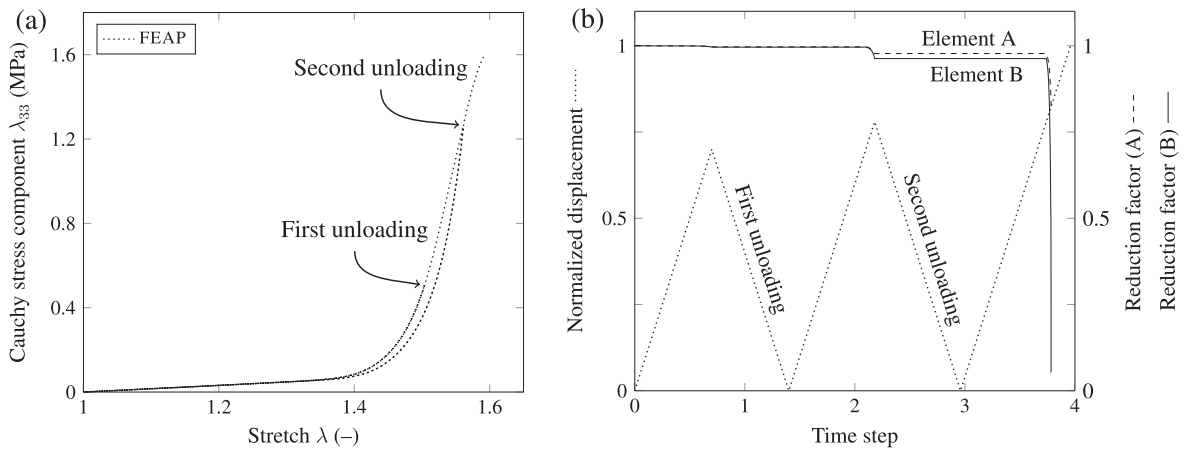


Fig. 12. Computational result of cyclic loading on the medial layer of the human thoracic aorta up to failure. (a) averaged Cauchy stress component σ_{33} versus the total stretch λ over the central elements (marked red in Fig. 11(a)), and (b) normalized displacement applied on the top face of the specimen and reduction factors at two elements A and B, see Fig. 11(a), versus the time step.

5. Concluding remarks

Recently, based on a systematic triangular discretization of a unit sphere, we demonstrated that the discrete fiber dispersion model is not only capable of excluding fibers under compression within a dispersion but can also efficiently approach the predictions of the CFD model (Li et al., 2018b) given enough density. In this study, we have extended the DFD model to account for the microscale fiber recruitment, softening and damage which are essential properties of collagen fibers.

For an efficient computational implementation, we decoupled the final form of the strain-energy function considering fiber recruitment and damage into volumetric and isochoric parts based on the multiplicative decomposition of the deformation gradient. We then presented corresponding analytical expressions of the Cauchy stress and elasticity tensors also in decoupled form. By using a mixed finite element formulation in FEAP and the augmented Lagrangian method for enforcing material incompressibility, we illustrated the capability and efficiency of the proposed DFD model with three numerical examples. For the first two examples, we have obtained very good agreement between the computational solutions obtained by using the proposed DFD model and the theoretical solutions obtained by using a modified version of the previously

developed CFD model (Li et al., 2016; 2018b). These results not only verified the finite element implementation of the proposed model but also indicated that the proposed discrete model is capable of modeling fiber recruitment, softening and damage in a way equivalent to that of the continuous approach under both extension and shear deformation. Due to the non-homogeneous deformation field that appeared in the last example, it was not possible to obtain a theoretical solution. Thus, we verified our computational solution with experimental data. With trial and error, we obtained a set of fiber parameters with which the computational solution agrees well with experimental data. For comparison, we also performed a computational analysis when fiber damage is not considered. Clearly, the results deviated from the actual experimental data after damage initiation. Further analysis of the dog-bone shaped specimen under cyclic loading revealed the effect of fiber damage on the unloading and re-loading responses of the proposed constitutive model.

In this study, we illustrated the capacity of the DFD method for modeling fiber recruitment by using a recruitment stretch in each fiber direction and fiber damage by using the CDM method and one type of damage evolution equation. Certainly, other methods of modeling fiber recruitment or fiber damage could also be considered in the DFD model. It is straightforward to implement other type of damage evolution equations as reviewed in Holzapfel and Fereidoonzhad (2017). Furthermore, the CDM method could be replaced by other methods, for example, by a failure stretch-based damage mechanism (Hadi et al., 2012).

In the last example, we approximated the 3D fiber dispersion in the specimen from the intensity plot measured at one location in the specimen. Certainly, the fiber dispersion may vary from region to region. We assume that this variation is small over the specimen. In addition, we assigned a set of random numbers within a range for the fiber recruitment stretches over the unit hemisphere. This treatment was motivated by the images of the fiber dispersion within the tissue obtained by using SHG. From those images, apparently, the fiber waviness does not follow any particular distribution pattern. Even on the same fiber, the waviness varies along the axial direction. For some fibers, we observed consistent waviness in one section, but at another section the fiber shows no waviness. In some region of the specimen, one fiber shows consistent waviness, but the adjacent fiber shows no waviness at all. Because one image only reveals the fiber waviness in a small region within the tissue, the overall 3D distribution of fiber waviness throughout the specimen is still unknown. If the 3D distribution of fiber recruitment stretch could be identified in an averaged sense, then we could also use that distribution together with DFD model in future studies. A realistic distribution of fiber waviness will certainly improve the accuracy of our model.

Finally, we believe that the capability of this novel discrete treatment of fiber dispersion is more than just excluding the compressed fibers within a dispersion as demonstrated in our previous study (Li et al., 2018a), and modeling of fiber recruitment and damage, as demonstrated in this study. Future studies considering patient-specific geometries in more complex boundary-value problems involving tissue growth and remodeling with the DFD model could further confirm this new approach.

Acknowledgments

We wish to thank Selda Sherifova, Graz University of Technology, for providing the uniaxial testing result and fiber dispersion data of the human thoracic aorta.

References

- Calvo, B., Peña, E., Martínez, M.A., Doblaré, M., 2007. An uncoupled directional damage model for fibred biological soft tissues. formulation and computational aspects. *Int. J. Numer. Meth. Engng.* 69, 2036–2057.
- Dassault Systèmes Simulia Corporation, 2017a. Abaqus analysis guide. Johnston, Rhode Island, United States.
- Dassault Systèmes Simulia Corporation, 2017b. Isight user's guide. Johnston, Rhode Island, United States.
- Dorfmann, A., Ogden, R.W., 2004. A constitutive model for the Mullins effect with permanent set in particle-reinforced rubber. *Int. J. Solids Struct.* 41, 1855–1878.
- Ehret, A.E., Itskov, M., Schmid, H., 2010. Numerical integration on the sphere and its effect on the material symmetry of constitutive equations—a comparative study. *Int. J. Numer. Meth. Engng.* 81, 189–206.
- Enea, D., Henson, F., Kew, S., Wardale, J., Getgood, A., Brooks, R., Rushton, N., 2011. Extruded collagen fibres for tissue engineering applications: effect of crosslinking method on mechanical and biological properties. *J. Mater. Sci. Mater. Med.* 22, 1569–1578.
- Fereidoonzhad, B., Naghdabadi, R., Holzapfel, G.A., 2016. Stress softening and permanent deformation in human aortas: continuum and computational modeling with application to arterial clamping. *J. Mech. Behav. Biomed. Mater.* 61, 600–616.
- Flory, P.J., 1961. Thermodynamic relations for highly elastic materials. *Trans. Faraday Soc.* 57, 829–838.
- Fung, Y.C., Fronek, K., Patitucci, P., 1979. Pseudoelasticity of arteries and the choice of its mathematical expression. *Am. J. Physiol.* 237, H620–H631.
- Gasser, T.C., 2011. An irreversible constitutive model for fibrous soft biological tissue: a 3-D microfiber approach with demonstrative application to abdominal aortic aneurysms. *Acta Biomater.* 7, 2457–2466.
- Gasser, T.C., Ogden, R.W., Holzapfel, G.A., 2006. Hyperelastic modelling of arterial layers with distributed collagen fibre orientations. *J. R. Soc. Interface* 3, 15–35.
- Gentleman, E., Lay, A.N., Dickerson, D.A., Nauman, E.A., Livesay, G.A., Dee, K.C., 2003. Mechanical characterization of collagen fibers and scaffolds for tissue engineering. *Biomaterials* 24, 3805–3813.
- Hadi, M.F., Sander, E.A., Barocas, V.H., 2012. Multiscale model predicts tissue-level failure from collagen fiber-level damage. *J. Biomech. Eng.* 134, 1–10.
- Hill, M.R., Duan, X., Gibson, G.A., Watkins, S., Robertson, A.M., 2012. A theoretical and non-destructive experimental approach for direct inclusion of measured collagen orientation and recruitment into mechanical model of the artery wall. *J. Biomech.* 45, 762–771.
- Holzapfel, G.A., 2000. Nonlinear solid mechanics. a continuum approach for engineering. John Wiley & Sons, Chichester.
- Holzapfel, G.A., Fereidoonzhad, B., 2017. Modeling of Damage in Soft Biological Tissues. In: Payan, Y., Ohayon, J. (Eds.), *Biomechanics of Living Organs. Hyperelastic Constitutive Laws for Finite Element Modeling*. Academic Press, pp. 101–123.
- Holzapfel, G.A., Gasser, T.C., Ogden, R.W., 2000. A new constitutive framework for arterial wall mechanics and a comparative study of material models. *J. Elast.* 61, 1–48.

- Holzapfel, G.A., Niestrawska, J.A., Ogden, R.W., Reinisch, A.J., Schriefl, A.J., 2015. Modelling non-symmetric collagen fibre dispersion in arterial walls. *J. R. Soc. Interf.* 12, 20150188.
- Holzapfel, G.A., Ogden, R.W., 2010. Constitutive modelling of arteries. *Proc. R. Soc. Lond. A* 466, 1551–1597.
- Holzapfel, G.A., Ogden, R.W., 2017. On fiber dispersion models: exclusion of compressed fibers and spurious model comparisons. *J. Elast.* 129, 49–68.
- Lanir, Y., 1983. Constitutive equations for fibrous connective tissues. *J. Biomech.* 16, 1–12.
- Lanir, Y., 2018. Multi-scale structural modeling of soft tissues: mechanics and mechanobiology. *J. Elasticity* 129, 7–48.
- Li, K., Ogden, R.W., Holzapfel, G.A., 2016. Computational method for excluding fibers under compression in modeling soft fibrous solids. *Eur. J. Mech. A/Solids* 57, 178–193.
- Li, K., Ogden, R.W., Holzapfel, G.A., 2018a. A discrete fibre dispersion method for excluding fibres under compression in the modelling of fibrous tissues. *J. R. Soc. Interf.* 15, 20170766.
- Li, K., Ogden, R.W., Holzapfel, G.A., 2018b. An exponential constitutive model excluding fibers under compression: application to extension-inflation of a residually stressed carotid artery. *Math. Mech. Solids* 23, 1206–1224.
- Li, K., Ogden, R.W., Holzapfel, G.A., 2018c. Modeling of fibrous biological tissues with a general invariant that excludes compressed fibers. *J. Mech. Phys. Solids* 110, 38–53.
- Li, K., Sun, W., 2017. Simulated transcatheter aortic valve deformation: a parametric study on the impact of leaflet geometry on valve peak stress. *Int. J. Numer. Method Biomed. Eng.* 33, E02814.
- Miyazaki, H., Hayashi, K., 1999. Tensile tests of collagen fibers obtained from the rabbit patellar tendon. *Biomed. Microdev.* 2, 151–157.
- Niestrawska, J.A., Viertler, C., Regitnig, P., Cohnert, T.U., Sommer, G., Holzapfel, G.A., 2016. Microstructure and mechanics of healthy and aneurysmatic abdominal aortas: experimental analysis and modeling. *J. R. Soc. Interf.* 13, 20160620.
- Ogden, R.W., 1978. Nearly isochoric elastic deformations: application to rubberlike solids. *J. Mech. Phys. Solids* 26, 37–57.
- Ogden, R.W., Roxburgh, D.G., 1999. A pseudo-elastic model for the Mullins effect in filled rubber. *Proc. R. Soc. Lond. A* 455, 2861–2877.
- Peña, E., 2011. Damage functions of the internal variables for soft biological fibred tissues. *Mech. Res. Commun.* 38, 610–615.
- Pins, G.D., Huang, E.K., Christiansen, D.L., Silver, F.H., 1995. Effects of static axial strain on the tensile properties and failure mechanisms of self-assembled collagen fibers. *J. Appl. Polym. Sci.* 63, 1429–1440.
- Rausch, M.K., Karniadakis, G.E., Humphrey, J.D., 2017. Modeling soft tissue damage and failure using a combined particle/continuum approach. *Biomech. Model. Mechanobiol.* 16, 249–261.
- Roy, S., Boss, C., Rezakhanlou, R., Stergiopoulos, N., 2010. Experimental characterization of the distribution of collagen fiber. *Recruitment* 24, 84–93.
- Sáez, P., Alastrué, V., Peña, E., Doblaré, M., Martínez, M.A., 2012. Anisotropic microsphere-based approach to damage in soft fibered tissue. *Biomech. Model. Mechanobiol.* 11, 595–608.
- Sang, C., Maiti, S., Fortunato, R.N., Kofler, J., Robertson, A.M., 2018. A uniaxial testing approach for consistent failure in vascular tissues. *J. Biomech. Eng.* 140, 061010.
- Schmidt, T., Balzani, D., 2016. Relaxed incremental variational approach for the modeling of damage-induced stress hysteresis in arterial walls. *J. Mech. Behav. Biomed. Mater.* 58, 149–162.
- Schmidt, T., Balzani, D., Holzapfel, G.A., 2014. Statistical approach for a continuum description of damage evolution in soft collagenous tissues. *Comput. Meth. Appl. Mech. Eng.* 278, 41–61.
- Schriefl, A.J., Wolinski, H., Regitnig, P., Kohlwein, S.D., Holzapfel, G.A., 2013. An automated approach for three-dimensional quantification of fibrillar structures in optically cleared soft biological tissues. *J. R. Soc. Interf.* 10, 20120760.
- Schriefl, A.J., Zeindlinger, G., Pierce, D.M., Regitnig, P., Holzapfel, G.A., 2012. Determination of the layer-specific distributed collagen fiber orientations in human thoracic and abdominal aortas and common iliac arteries. *J. R. Soc. Interf.* 9, 1275–1286.
- Shah, S.B., Witzenburg, C., Hadi, M.F., Wagner, H.P., Goodrich, J.M., Alford, P.W., Barocas, V.H., 2014. Prefailure and failure mechanics of the porcine ascending thoracic aorta: experiments and a multiscale model. *J. Biomech. Eng.* 136, 021028–1.
- Simo, J.C., 1987. On a fully three-dimensional finite-strain viscoelastic damage model: formulation and computational aspects. *Comput. Meth. Appl. Mech. Eng.* 60, 153–173.
- Simo, J.C., Taylor, R.L., 1991. Quasi-incompressible finite elasticity in principal stretches. continuum basis and numerical algorithms. *Comput. Meth. Appl. Mech. Eng.* 85, 273–310.
- Sommer, G., Sherifova, S., Oberwalder, P.J., Dapunt, O.E., Ursomanno, P.A., De Anda, A., Griffith, B.E., Holzapfel, G.A., 2016. Mechanical strength of aneurysmatic and dissected human thoracic aortas at different shear loading modes. *J. Biomech.* 49, 2374–2382.
- Taylor, R.L., 2013. FEAP – A Finite Element Analysis Program, Version 8.4 User Manual. University of California at Berkeley. Berkeley, California.
- Volokh, K.Y., 2007. Hyperelasticity with softening for modeling materials failure. *J. Mech. Phys. Solids* 55, 2237–2264.
- Volokh, K.Y., 2008. Prediction of arterial failure based on a microstructural bi-layer fiber–matrix model with softening. *J. Biomech.* 41, 447–453.
- Volokh, K.Y., 2011. Modeling failure of soft anisotropic materials with application to arteries. *J. Mech. Behav. Biomed. Mater.* 4, 1582–1594.
- Weisbecker, H., Unterberger, M.J., Holzapfel, G.A., 2015. Constitutive modelling of arteries considering fibre recruitment and three-dimensional fibre distribution. *J. R. Soc. Interf.* 12, 20150111.
- Weisbecker, H., Viertler, C., Pierce, D.M., Holzapfel, G.A., 2013. The role of elastin and collagen in the softening behavior of the human thoracic aortic media. *J. Biomech.* 46, 1859–1865.
- Zuo, K., Pham, T., Li, K., Martin, C., He, Z., Sun, W., 2016. Characterization of biomechanical properties of aged human and ovine mitral valve chordae tendineae. *J. Mech. Behav. Biomed. Mater.* 62, 607–618.